

Title	Epitaxial post-implant recrystallization in germanium nanowires
Authors	Kelly, Róisín A.;Liedke, Bartosz;Baldauf, Stefan;Gangnaik, Anushka S.;Biswas, Subhajit;Georgiev, Yordan M.;Holmes, Justin D.;Posselt, Matthias;Petkov, Nikolay
Publication date	2015-08-14
Original Citation	Kelly, R. A., Liedke, B., Baldauf, S., Gangnaik, A., Biswas, S., Georgiev, Y., Holmes, J. D., Posselt, M. and Petkov, N. (2015) 'Epitaxial Post-Implant Recrystallization in Germanium Nanowires', Crystal Growth & Design, 15(9), pp. 4581-4590. doi: 10.1021/acs.cgd.5b00836
Type of publication	Article (peer-reviewed)
Link to publisher's version	http://pubs.acs.org/journal/cgdefu - 10.1021/acs.cgd.5b00836
Rights	© 2015 American Chemical Society. This document is the unedited Author's version of a Submitted Work that was subsequently accepted for publication in Crystal Growth & Design, copyright © American Chemical Society after peer review. To access the final edited and published work see https://pubs.acs.org/doi/10.1021/acs.cgd.5b00836
Download date	2025-04-04 07:08:37
Item downloaded from	https://hdl.handle.net/10468/6577



UCC

University College Cork, Ireland
 Coláiste na hOllscoile Corcaigh

Epitaxial post-implant recrystallization in Germanium nanowires

*Roisin A. Kelly,[†] Bartosz Liedke,[§] Stefan Baldauf,[§] Anushka Gangnaik,[†] Subhajit Biswas,[†]
Yordan Georgiev, Justin D. Holmes,^{†‡} Matthias Posselt,[§] Nikolay Petkov^{†*}*

[†]Materials Chemistry and Analysis Group, Tyndall National Institute and the Department of Chemistry, University College Cork, Ireland.

[§]Helmholtz Zentrum Dresden Rossendorf, Institute of Ion Beam Physics and Materials Research, Dresden, Germany.

[‡]Centre for Research on Adaptive Nanostructures and Nanodevices (CRANN), Trinity College Dublin, Dublin 2, Ireland.

KEYWORDS: Recrystallization, Germanium, nanowire, ion irradiation, defect

ABSTRACT: As transistor dimensions continue to diminish, techniques for fabrication need to be adapted. In particular, crystal recovery post ion implantation is required due to ion bombardment inducing amorphisation. Here, we report a study on the post implant

recrystallization in germanium (Ge) nanowires (NWs) following gallium (Ga) ion doping. In this work, a variation of NW diameters and orientations were irradiated and annealed in-situ to investigate the mechanism of recrystallization. An added complication of misorientation of crystal grains increases the complexity of crystal recovery. It has been shown that when the misorientation is prevented, by leaving a crystal link between two seeds and providing a rigid support, recrystallization occurs primarily via solid phase epitaxial growth. This work highlights both experimentally and through molecular dynamic simulations the importance of engineering crystal recovery in Ge NWs which may have potential for next-generation complementary metal-oxide semiconductor (CMOS) devices.

INTRODUCTION

Keeping on trend with Moore's law has seen a demand for smaller and more efficient transistor devices. The development of future "More-than-Moore" and beyond CMOS technologies with breakthroughs in nanometer-sized function require alternative materials.¹ Due to its higher intrinsic mobilities and larger exciton Bohr radius than Si, Ge is reemerging as a promising candidate to replace or integrate with Si.²⁻³ Accurate control of doping is vital when fabricating NW FETs⁴⁻⁵ and other NW devices such as sensors,⁶⁻⁷ photovoltaics⁸ and photonics devices.⁹ Ion beam doping is currently common practice but transferring this technique to nanostructures is challenging. The destructive nature of ion beam doping due to ion bombardment and resultant cascade recoils within the NW volume means a crystal recovery step is required.¹⁰

An increase in conductivity has been demonstrated in grown Ge NWs irradiated with a Ga ion source up to a fluence of $6.25 \times 10^{12} \text{ cm}^{-2}$ without an activation (annealing) step.¹¹ Above this

fluence, a drop in conductivity is observed and is attributed to amorphisation. However, higher implantation fluences are required to achieve the proper function of advanced transistors such as NW junctionless FETs¹² and photonic devices.¹³⁻¹⁴ Unfortunately full recovery of irradiated nanostructures is not easily achievable.^{10, 15}

There has been an extensive body of research investigating the recrystallization of bulk Ge and some progress in recent years on Si and Ge nanostructure recrystallization post ion irradiation.^{10, 15-20} The high surface-area to volume ratio in nanostructures results in a greater sensitivity to surface roughness and possible surface over-layers.^{18,19} Stacking faults nucleate at dangling bonds found at sidewalls and surfaces.^{10, 15} Nanowires possess high surface area to volume ratios, therefore dangling bonds, and by extension stacking faults, are prevalent. The bulk material acts as a seed for the recrystallization of fin structures and nanopillars via solid phase epitaxial growth (SPEG), however, a polycrystalline region is observed to occur at the top of the structure (i.e. not in proximity to the bulk crystal seed).^{15, 18} This polycrystalline region is likely due to the predominance of random nucleation and growth (RNG). NWs, with no contact to a bulk substrate, which undergo ion irradiation along its entire length, and hence experience full amorphisation, lack the seed which facilitates SPEG and hence recrystallization occurs solely via RNG. Another undesirable factor which affects the recrystallization of NWs is loss of rigidity (bending) with ion bombardment induced amorphisation. A misorientation between two crystalline fronts results in a crystal mismatch and hence defect formation.²¹ It has been shown that NWs can be bent in a desired direction depending on the energy and the direction of the incoming ion beam.^{19, 22-23} Bending occurs to minimize stress within the NW due to amorphisation. The stress may be due to formation of a crystalline/amorphous (c/a) interface,¹⁹ a combination of compressive and tensile stress due to formation of vacancies and interstitials,²³ or

it may be due to densification during irradiation.²² Importantly, the influence of the topology of the c/a interface and the rigidity (bending) of the NW on high temperature regrowth has not been investigated.

An understanding of the recrystallization process will aid in the engineering of defect-free highly doped nanostructures. Experimental data coupled with modelling calculations have already shown the dependence of crystal orientation for the rate of recrystallization.^{15, 24-26} In this work, a detailed investigation into Ge NW recrystallization post Ga-ion irradiation by in-situ TEM combined with molecular dynamics calculations is presented. The main aim of this study is to devise a method to reduce residual defects after recrystallization in Ge NWs. By minimizing the contribution of RNG and the role of misorientation in the recrystallization fronts due to NW bending, a predominately SPEG mechanism and defect-free regrowth is promoted. It is demonstrated that NW partial amorphisation allows for single crystal seed remnants which facilitate SPEG recrystallization. For the investigation of the role of misorientation of crystal seeds for regrowth, NWs were encapsulated in an external amorphous matrix on a flat wafer support to preserve their rigidity during irradiation. Combining these approaches, post-anneal Ga-ion implanted Ge NWs (with implantation doses up to $4.8 \times 10^{15} \text{ cm}^{-2}$) with no apparent stacking fault defects were demonstrated on buried oxide.

EXPERIMENTAL AND SIMULATION

The method for platform preparation, concurrent imaging and doping of NWs using a dual beam focused ion beam (FIB) and scanning electron microscope (SEM) has been described previously.¹⁰ For accurate selective area doping within a section of single NW it is important to

align the electron and ion beam coincident point precisely as the exposure needs to be done “blind” with the aid of the electron beam for navigation. A 30 keV Ga ion beam, operating at a current of 9.6 pA, was used for all implantation experiments presented here. A rectangle area is defined for the irradiations. The length of the NWs irradiated varied between 200 nm and 1 μm . The typical area irradiated was 200 nm (along length of NW) \times 5 μm . A minimum dose of 1.9×10^{13} ions cm^{-2} was used in the experiments presented here. Small areas can be accurately irradiated with Ga ions without introducing impurities to the surrounding structures by using a well-aligned FIB.

An overview of the experimental procedure for the irradiation and imaging of NWs is depicted in a schematic in Figure 1. NWs deposited on silicon nitride membranes do not require any additional steps for observing the damage incurred and subsequent in-situ TEM annealing (Figure 1 a).¹⁰ For the NWs on a substrate, grown NWs deposited on a Si/SiO₂ chip via dry transfer from the growth substrate or electron beam lithography (EBL) defined NWs on GeOI (germanium on insulator) were used.²⁷⁻²⁸ In order to observe the in-situ TEM recrystallization along the NWs on substrates, the structures need to be extracted with the underlying substrate (Figure 1 iii). This is done via a non-typical inline FIB lift-out technique along the NW length (SI Fig S1). For all NWs imaged on silicon nitride membranes, the direction of the ion beam (red arrow) during irradiation is nearly parallel to the electron beam (purple arrow) when imaged in the TEM (Figure 1 a). However, for NWs extracted from a substrate (Figure 1 b) the direction of the ion beam is orthogonal to the direction of the electron beam when imaged in the TEM, i.e. we have a side view of the irradiated NW along its length. The GeOI NWs defined by EBL have a height of approximately 50 nm, which is almost twice the range of interactions of the 30 kV Ga-ions in Ge. Therefore, to achieve amorphisation across the NW (the width of the NWs is

approximately 40 nm) and avoid ion channeling, very high ion-beam incidence angles ($\pm 62^\circ$) were used.

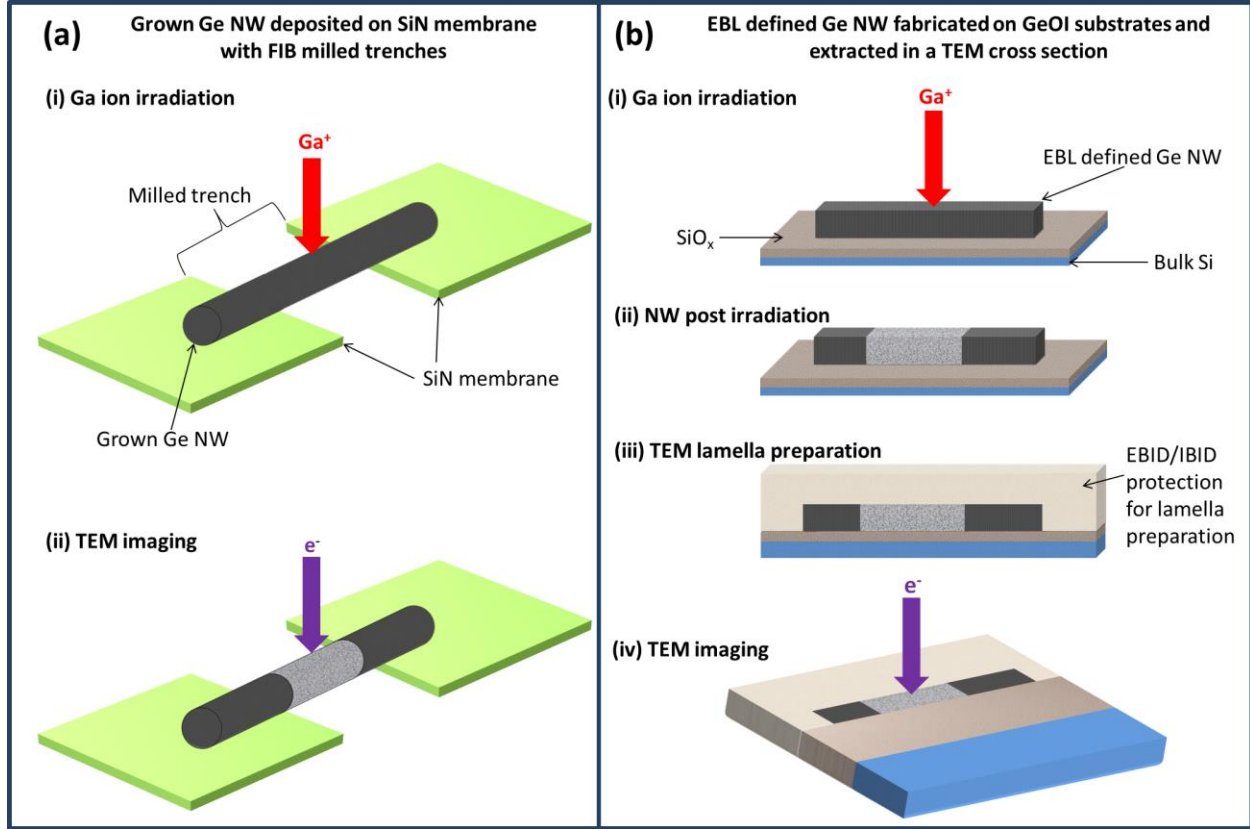


Figure 1. Schematic overview of sample preparation and imaging for (a) a nanowire on pre-patterned SiN membrane and (b) EBL defined NW from on GeOI substrate.

An in-situ Gatan Model 628 single-tilt heating stage TEM holder was used for all anneals presented in this study. The ramp/temperature used for each NW varied. The sample was loaded in the same orientation in the in-situ heating stage as it was for HRTEM imaging in the double tilt holder. The in-situ heating stage is only capable of single tilt so the sample was tilted as close to the zone axis used for high resolution imaging as possible. For most samples tilting in two directions is required to achieve a zone axis orientation for lattice resolution imaging. The TEM was operated in bright field z-contrast mode, isolating the direct beam with the objective

aperture, to take advantage of the contrast between the crystalline and amorphous regions. Temperature was controlled using a Gatan Model 901 SmartSet hot stage controller. Temperatures varied from 100 – 500 °C. Images were acquired every minute.

In order to better understand experimental results molecular dynamics (MD) simulations on recrystallization of a-Ge NWs were performed. In this study we employed the LAMMPS program²⁹ with a Stillinger-Weber-type interatomic potential.³⁰ The simulation cell used for the calculation were cuboids with a size of $20 \times 20 \times 30 a^3$ and $20 \times 20 \times 60 a^3$, i.e. initially with a total of 96000 and 192000 atoms, respectively, where $a = 5.657 \text{ \AA}$ is the lattice parameter of c-Ge. Simulation cells with long sides parallel to the $\langle 111 \rangle$ and the $\langle 100 \rangle$ crystal axes were considered in order to study NWs with these orientations. Periodic boundary conditions in three directions and a canonical ensemble (NVT) were used. The amorphous region was prepared by the method of Luedtke et al.³¹ via slow cooling from the melt at a rate of 1 K ps^{-1} , analogically to the work of Posselt et al.³⁰ To obtain a NW with free surfaces in x- and y-directions, all atoms within the distance of $5a$ from the x,y-borders of the simulation cell were removed. The resulting systems with 24000 (for $20 \times 20 \times 30a^3$ simulation cell) and 48000 atoms (for $20 \times 20 \times 60a^3$ simulation cell) consist of two c/a interfaces as shown in Figure 4(a) and Figure 5(a). In recrystallization calculations at 700, 750, 800, and 900 K (426.85, 476.85, 526.85, and 626.85 °C, respectively) a Berendsen thermostat was used.³² Zero pressure (stress) was maintained at the cell boundaries in both z-directions using a Berendsen barostat.

RESULTS AND DISCUSSION

Figure 2 (a) and (b) show TEM images of a 38 nm diameter $\langle 111 \rangle$ grown NW (NW1), imaged along the $[\bar{2}11]$ zone axis, irradiated to induce full amorphisation in a 200 nm section of the NW length. Note that the NW is suspended across an open trench of the silicon nitride membrane. A misorientation is observed between the two crystalline regions, X and Y, separated by the amorphous region which is approximately 205 nm in length. The two crystalline regions were estimated to be at a relative angle (θ) of approximately 3° to each other.³³ Although only a small region experienced full amorphisation, partial amorphisation/damage occurred a further 300 nm at either side.

In-situ annealing of the NW was observed in the TEM at 400 °C for 83 min and subsequently at 450 °C for 37 min (Figure 2 f). Because there was a misorientation of the two crystal seeds only one seed was selected for observation during the anneal process. Within the first 25 min of the anneal, the damaged region, which experienced partial amorphisation and contains many crystallites, developed a continuous crystal growth front (Figure 2 (f) at 25 min). The recrystallization appears to occur preferentially along the length and in the center of the NW forming an arrow-head type crystal front. As the crystal front approaches a fully amorphous region, the crystal front flattens, which is expected as growth in the $\langle 111 \rangle$ direction is least favorable.³⁴ The arrow-head recrystallization front is observed again when the temperature is increased to 450 °C (and the rate in turn increases) until a point when the front meets region Z. The recrystallization rate was estimated by measuring the crystalline region from the images acquired during the anneal. See SI Fig S2 for the analytical procedure adopted to determine crystal re-growth rates by the TEM images acquired.

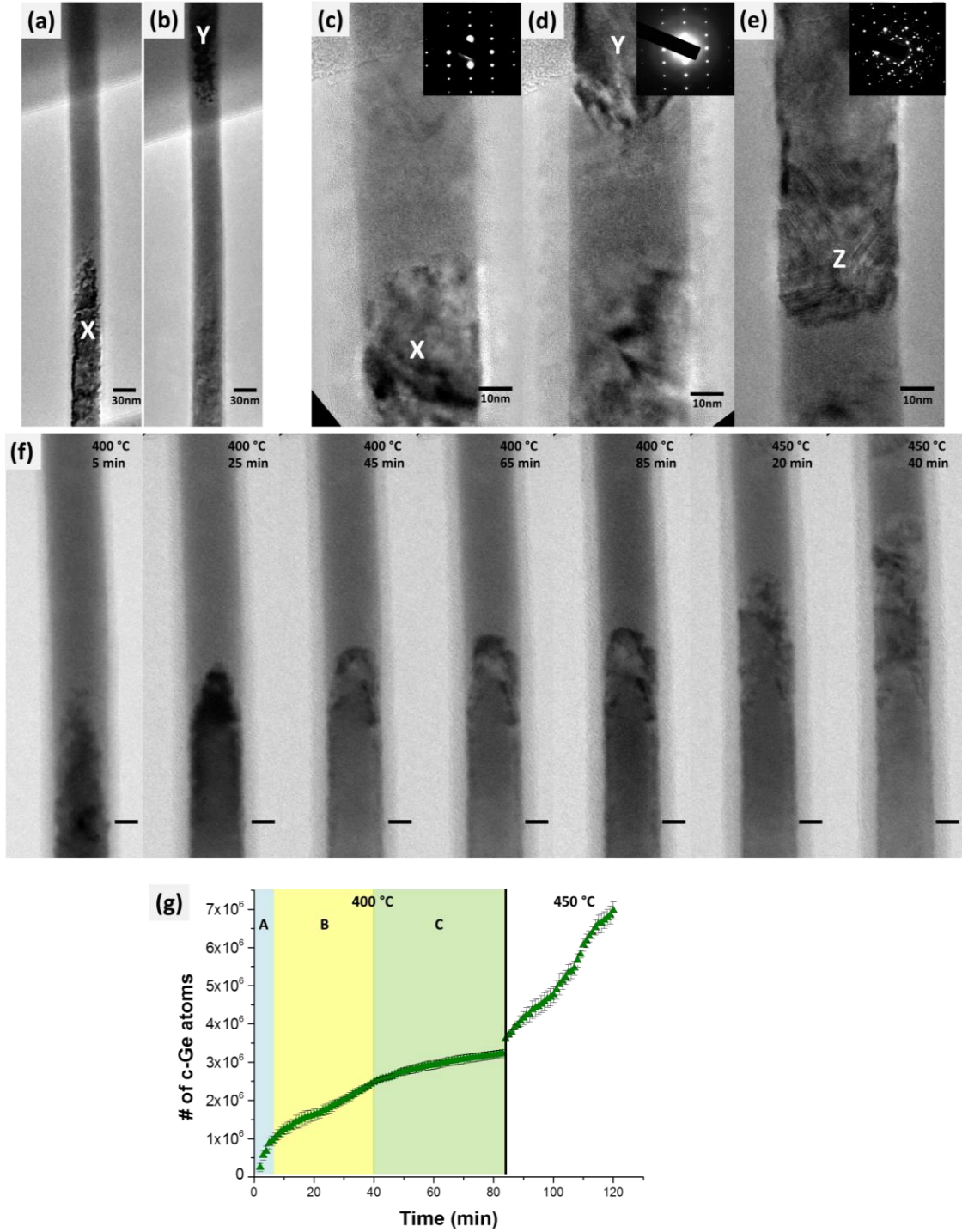


Figure 2. NW1 after irradiation to only part of the length which experiences full amorphisation, (a) and (b). Post anneal, different crystalline regions, (c), (d) and (e). Different tilts are required to orient regions X, Y and Z into zone axis. Before the anneal (a and b) regions X and Y are approximately 3° relative to each other. After the anneal (c-e) regions X and Y maintain the misorientation with a relative angle of 4.2° and the third region Z is at a relative angle of 17° and 14.7° to X and Y, respectively. (f) In-situ anneal of NW1 at 400°C for 83 min and a further 37 min at 450°C . Scale bar is 5nm. (g) Graphical representation of recrystallization of NW1.

A graphical representation of the calculation results is presented in Figure 2 (g). A description of the calculation method used to calculate the rates of crystallization presented here have been included in the Supporting Information. The measurements were completed at least three times to achieve a statistically correct overview. It can be observed that a constant rate is not observed for the duration of the 400 °C anneal. The initial recrystallization rate for the first 5 min was approximately 3404.75 atoms s⁻¹ (Figure 2 (g) region A), which decreased to 696.33 atoms s⁻¹ for minutes 6-40 (region B) after which the rate dropped again to 281.5 atoms s⁻¹ (region C). The recrystallization rate after the temperature increase to 450 °C rose again to 1591.5 atoms s⁻¹. The initial high recrystallization rate is postulated here to be due to the higher number of mono-oriented and connected crystalline seeds within the partially damaged region which act as preferential growth sites.³⁴ Similar deviation from linear growth has been observed previously for Ge and particularly for short anneal times for thin amorphous layers which has been attributed to void formation or the introduction of oxygen during the anneal.³⁵ In another study, by Johnson et al, it was shown that the rate of SPEG decreased as the growth front approached within 0.3 μm of the surface and has been attributed to H infiltration.³⁶ Johnson et al also showed that the H infiltration has a higher impact on Ge than Si SPEG.

Figure 2 (c), (d) and (e) show HRTEM images of the recrystallized NW after annealing. The mismatch of the two crystal planes was retained with the formation of a highly defective region between the two crystal grains, region Z. The relative angles for the crystal grains imaged were calculated; $\theta_{XY} = 4.2^\circ$; $\theta_{YZ} = 17^\circ$; $\theta_{XZ} = 14.7^\circ$. The region between grains X and Y appears to be amorphous but when imaged in the zone axis for Z it is clear that it is in fact crystalline. The formation of the defective grain (Z) is highly irregular. The smallest possible angle between $\langle 211 \rangle$ and $\langle 011 \rangle$ is 30° (SI Eq1). A plausible explanation for this unexpected grain formation

is RNG in the strained region. Regions X and Y have maintained the original crystallographic relationship with a misorientation between the two regions. However, region Z has no rational crystallographic relationship with either regions X or Y indicating a polycrystalline growth due to RNG. It has been shown that a NW can be bent in a desired direction upon FIB exposure and maintains the bent shape even after high temperature annealing.^{19, 22-23} The result for NW1 correlates well with results on Si NW recrystallization published by Pecora et al in which NWs were irradiated and experienced bending.¹⁹ Some NWs, presented by Pecora et al, straightened during recrystallization and were single crystalline, albeit partially defective, but NWs which remain bent were polycrystalline. Summarizing the mechanism of recrystallization for the suspended Ge NW1 (Figure 2) two different regrowth mechanisms can be identified (single crystalline vs polycrystalline) with SPEG resulting in the single crystalline regrowth from regions X and Y, and RNG resulting in the polycrystalline regrowth in region Z.

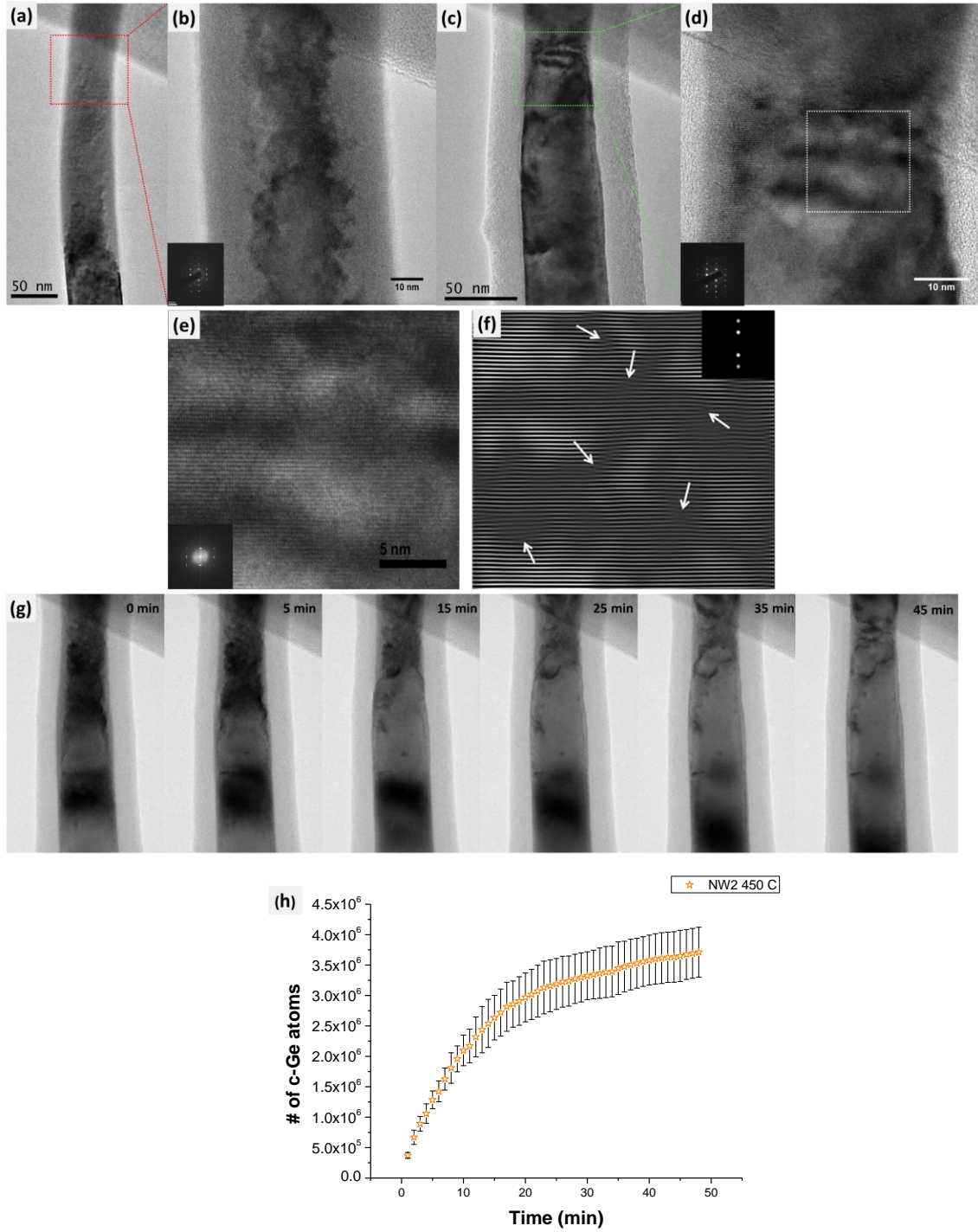


Figure 3. NW2 (a) and (b) partially irradiated with remaining crystal in irradiated region imaged in (211) zone axis. (c) and (d) after annealing at 400 °C for 47 min. (e) A high resolution lattice image of region identified in (d). (f) Inverse of (211) reflections from FFT of (e). White arrows indicate mis-fit dislocations. (a) In-situ anneal of 64 nm Ge NW (NW2) at 400 °C for 47 min. (b) Graphical representation of recrystallization.

A (larger) 56 nm diameter $\langle 111 \rangle$ grown NW also imaged in $[\bar{2}11]$ zone axis was irradiated to induce amorphisation but retain a crystalline “backbone” for a section of the NW across an open trench of a silicon nitride membrane (

Figure 3) (NW2). A cross section of another irradiated 50 nm $\langle 111 \rangle$ grown NW has been presented in SI Fig S3. Depending on the energy of the ion beam, the range of the ions can be estimated.³⁷ In this case, a 30kV Ga ion beam does not have enough energy to penetrate and induce cascade recoils through the whole diameter of the NW and hence a crystal region remains along the back of the NW. This backbone provides a support for the NW, maintaining some rigidity by preventing misorientation and allowing a direct link between the two non-irradiated regions. It is observed in

Figure 3 (a) that the NW experiences some bending. The only way to avoid this bending for a grown NW is to provide a flat and stable support, e.g. on Si_3N_4 or SiO_2 substrate. In-situ annealing was observed in the TEM at 400 °C for 47 min (

Figure 3 g).

An estimation of the recrystallization rate is represented graphically in

Figure 3 (h). When recrystallization occurred in the NW1 in Figure 2 there was a clear interface between the crystalline and amorphous regions. In

Figure 3 (a) and (b), the volume of the amorphous region is not quantifiable based on the images alone. Thus, the estimation of the recrystallization rate from

Figure 3 (g) is an underestimation of the rate and volume of Ge recrystallized. The initial recrystallization rate for the first 15 min is estimated to be $3130 \text{ atoms s}^{-1}$. HRTEM images post-anneal show a monocrystalline NW (

Figure 3 c-e). No stacking fault defects are observed along the growth direction of the NW imaged in the $[\bar{2}11]$ zone axis. From the reconstructed FFT (

Figure 3 f), the presence of dislocations in the crystal can be identified (white arrows), these are likely to be stacking faults on the $(\bar{1}11)$, $(1\bar{1}1)$ and/or $(11\bar{1})$ planes. To confirm these “hidden defects” it would be required to tilt to another zone axis such as the $[011]$ zone axis.³⁸

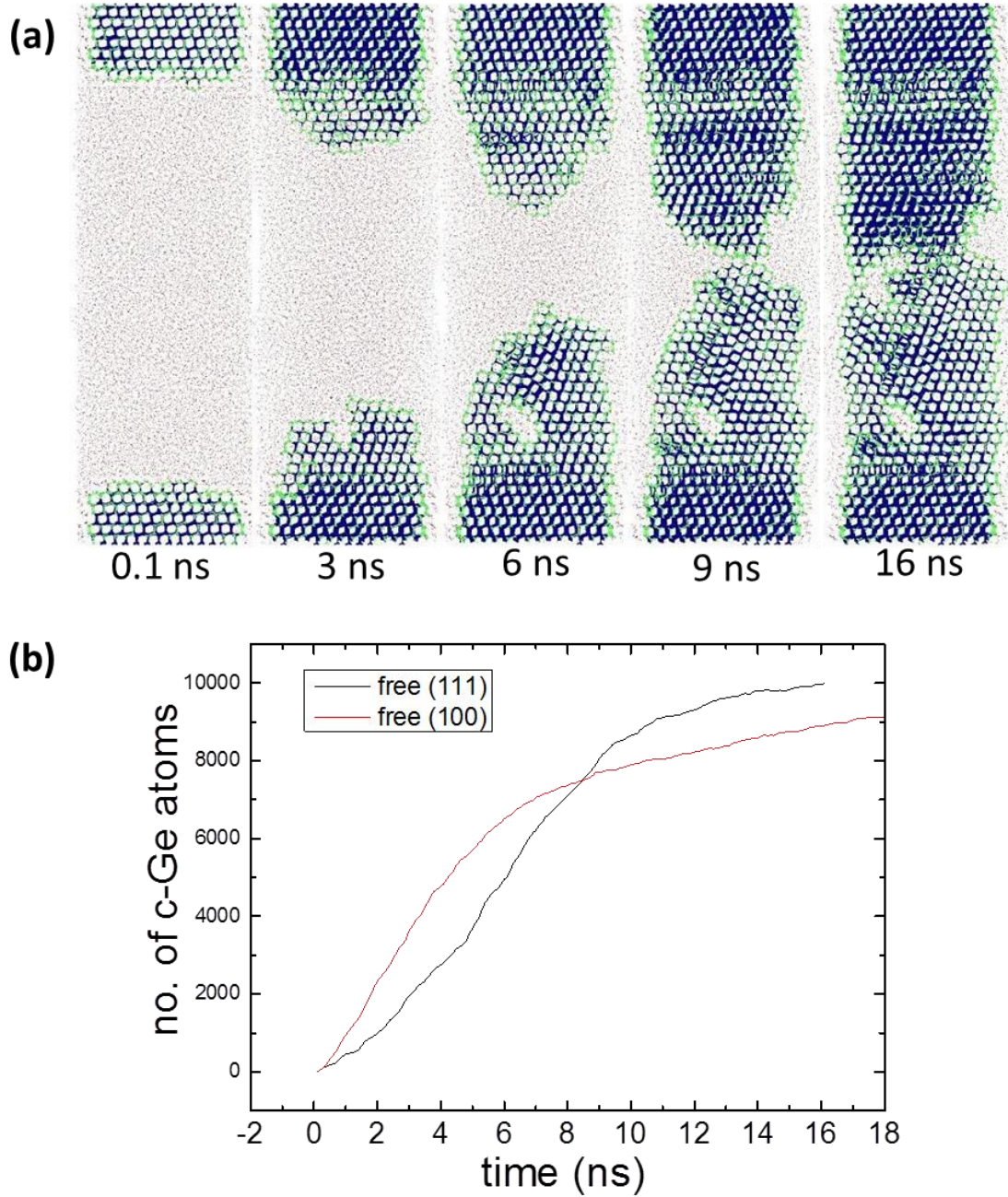


Figure 4. (a) Molecular dynamics simulation of recrystallization of a (111) grown Ge NWs at 800K. (b) Comparison of SPR of NWs for two orientations (100) and (111) shows a very similar growth rate using MD calculations. Simulation cell size is $20 \times 20 \times 30a^3$, where $a = 5.657 \text{ \AA}$ in both figures.

Molecular dynamics (MD) calculations are presented in Figure 4 for a $\langle 111 \rangle$ grown NW. The notable comparison between the MD calculations and the experimental results is the general

shape of the recrystallization curve; initial higher rate, followed by a decrease in the re-growth. From the MD calculations, it can be observed that the initial growth rate is approximately 1×10^{12} atoms s^{-1} but the overall observed rate for the time (16ns) is approximately 6×10^{11} atoms s^{-1} which is a drop to 60% of the initial rate. The absolute values of simulated recrystallization rates are larger than the measured data. This is related to the quality of the interatomic potential used in the calculations, which was designed to reproduce realistic properties of crystalline, amorphous and liquid Ge but does not describe SPEG quantitatively correct. Therefore the comparison with experimental results is focused on general trends regarding the recrystallization process.

MD calculations have also been presented for a $\langle 001 \rangle$ grown nanowire in Figure 5. Three different rates of SPR (solid phase recrystallization) are visible for each curve, except 700 K annealing, where saturation has not yet been achieved. Decrease of the regrowth rate in the first few ns of annealing for each temperature suggests a considerable importance of confinement effects. The rates decrease again after the two fronts of recrystallization meet in the middle of the supercell. The thick lines are the linear fits applied for the initial slopes, used to calculate activation energy of SPEG that equals 0.92 eV.

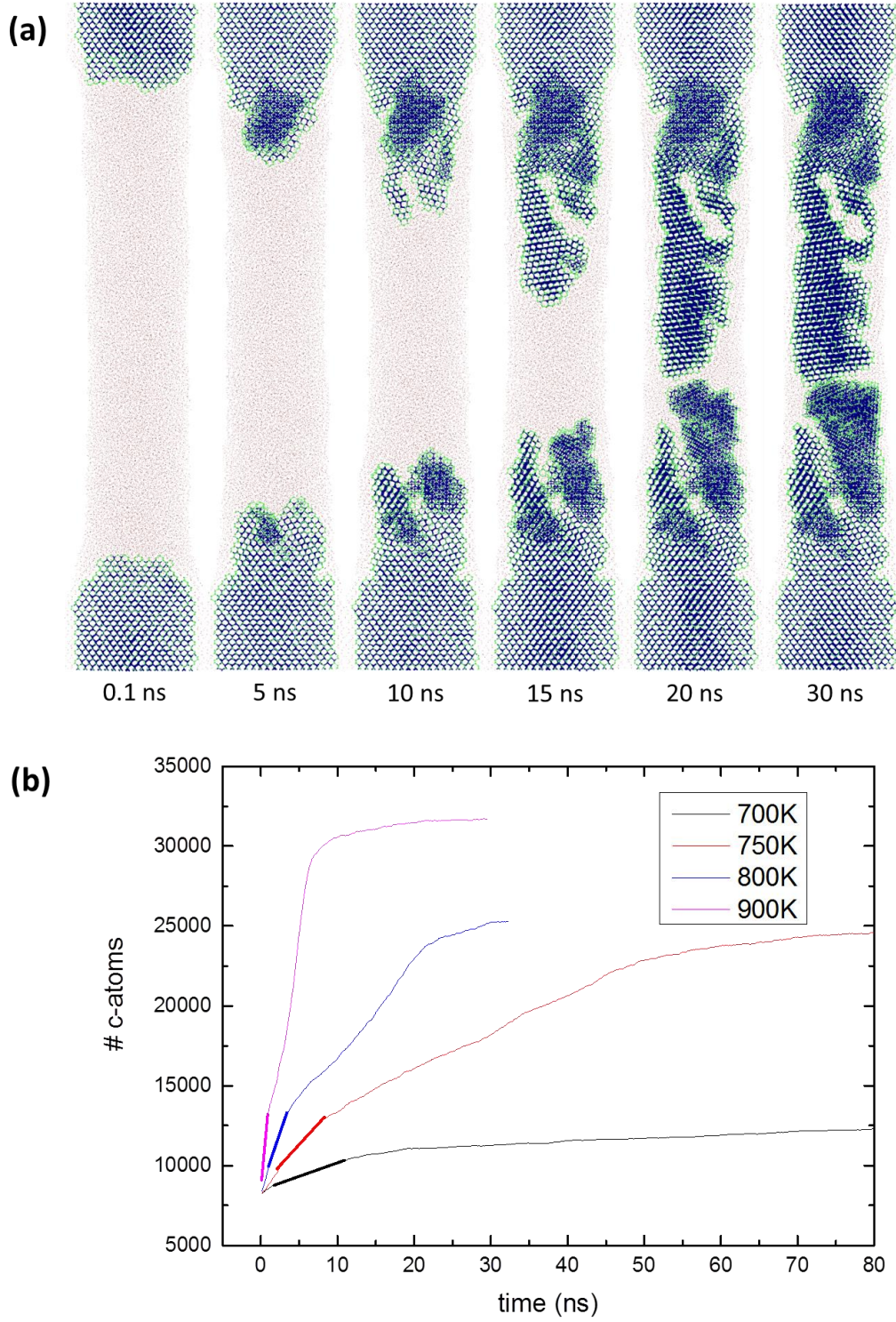


Figure 5. (a) (100)-growth in Ge NW at T=800K (b) (100) growth in Ge NWs at varied T: 700K, 750K, 800K and 900K. Simulation cell size is $20 \times 20 \times 60a^3$, where $a = 5.657 \text{ \AA}$ in both figures.

In an attempt to reduce and understand the influence of strain experienced by a suspended NW, a NW deposited on a substrate was irradiated, encapsulated and recrystallized in-situ (Figure 6) (NW3). The 64 nm diameter, $\langle 211 \rangle$ grown NW containing intrinsic (111) stacking faults along the NW length, was irradiated on a Si/SiO₂ substrate and then extracted as an inline FIB cross-section, i.e. along its length. In this method, the NW is encapsulated in EBID (electron beam induced deposition) carbon. A section approximately 500 nm along the NW was defined for irradiation but a length of approximately 600 nm experienced amorphisation (Figure 6). As observed in Figure 6 (a), only partial amorphisation across the NW diameter is achieved leaving a continuous backbone similarly to the NW2. The embedded NW was annealed in-situ at 400 °C for 30 min (Figure 7). It is clear from the images taken in-situ that the recrystallization occurs epitaxially, i.e. via a SPEG mechanism.

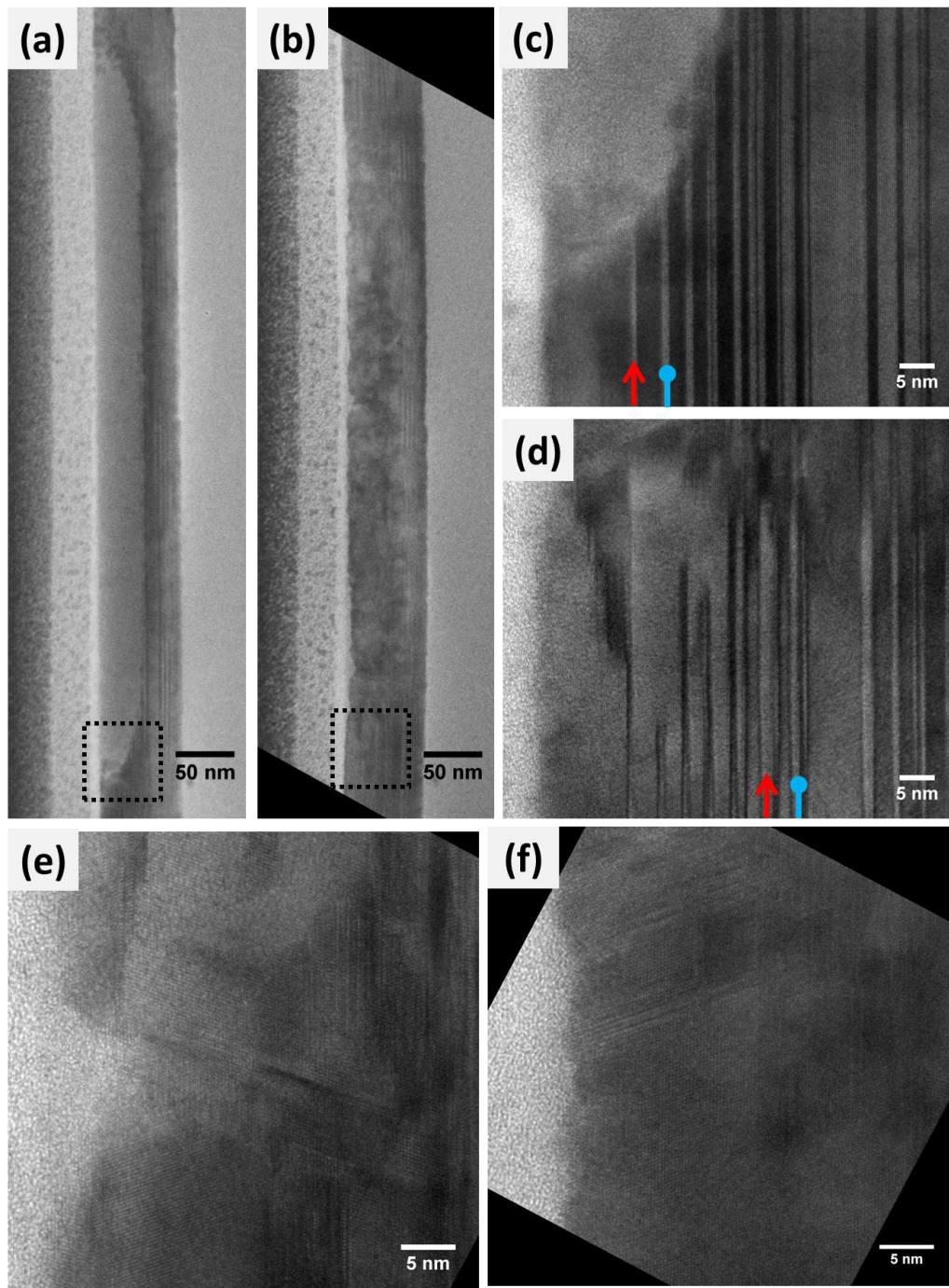


Figure 6. (211) grown NW3 (a) after irradiation and (b) after anneal at 400 °C for 30 min. (c) and (d) are high resolution images from (a) and (b) respectively. HRTEM of recrystallized NW3. A combination of (111) stacking faults pinned to the surface, stacking faults parallel to intrinsic defects and defect free regions.

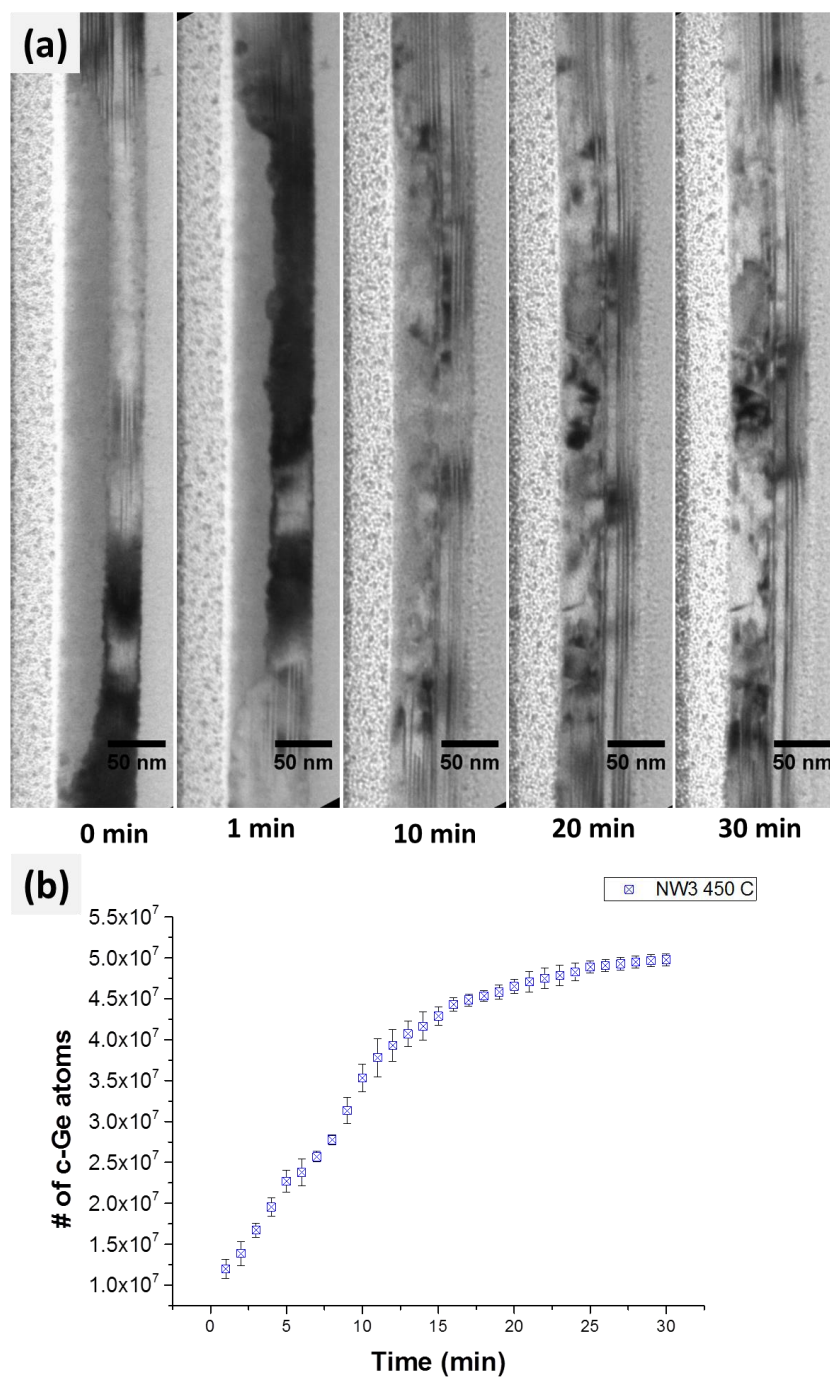


Figure 7. In-situ anneal of NW3 at 400 °C for 30 min. Graphical representation of Ge recrystallization during the anneal of NW3.

Two major crystal fronts can be identified; one in the (111) direction orthogonal to the NW long axis, which is the larger growth front, and the other growth front in (211) direction, i.e. the NW growth direction. HRTEM images post-anneal show a mixture of defect curing, intrinsic defect propagation as well as the appearance of newly formed (extrinsic) defects (Figure 6 e and f). Some of the extrinsic defects formed are ($\bar{1}11$) stacking faults in the same direction as the intrinsic defects (along the NW length) and the rest are (111) stacking faults which are pinned to the NW surface. Interestingly, the region towards the middle of the amorphous area recrystallized with the formation of mainly extrinsic stacking faults. The intrinsic defect propagation is limited to the edges of the damaged region. The recovery of intrinsic stacking faults from a fully amorphous structure, i.e. the phenomenon of crystal memory, has not been observed. However, seeding of parallel stacking faults through defects in the Au seed and their propagation along the (211) grown Ge NWs has been reported.³⁹ In Figure 6 (d), the newly formed stacking faults appears random but on closer inspection of the c/a interface before the anneal, the roughness can be attributed to the variation in the propagation of the stacking faults. For stacking fault 1 (SF1) (indicated with red arrows in Figure 6), there is a damaged region which has not experienced full amorphisation, this is due to cascade recoils being ejected from the NW volume.^{10, 17} A broadening is observed for SF1 grain in Figure 6 (d) post anneal. This migration has been previously observed and is attributed to the slower growth rate in $\langle 111 \rangle$ than in the $\langle 511 \rangle$ direction, resulting in a migration of the twin grain in a stepwise fashion.⁴⁰ Stacking fault 2 (SF2) (indicated with blue pins in Figure 6) c/a interface is sharp with little or no ordering present. The bulk crystal grain engulfs the stacking fault and effectively prevents propagation of the stacking fault in the (211) growth direction. This illustrates the importance of the roughness of the c/a interface. An initial recrystallization rate of $39046 \text{ atoms s}^{-1}$ was

estimated for the first 15 min based on the images from the in-situ anneal. As observed for the previous two anneals, the rate begins to level off as the NW recrystallizes fully.

A (001) Ge NW on insulator with rectangular cross-section (width 40 nm, height 55 nm) defined via electron beam lithography (EBL) was irradiated and annealed in-situ (Figure 8) (NW4). Irradiation was done at high incidence angles ($\pm 62^\circ$, i.e. -10° tilt of the stage) to induce amorphisation as the width of the NW is less than the height of the GeOI. Annealing was initiated at 100 °C with incremental increases in steps of 50 °C every 15 min. Notable recrystallization was only observed from 400 °C. Recrystallization rates were extracted from the in-situ images for 400 and 450 °C, 3479 and 18566 atoms s⁻¹, respectively (Figure 8). The initial heating rate affects the recrystallization temperature observed.⁴¹ Estimation of the recrystallized volume is more accurate as the cross sectional shape of GeOI NW is rectangular (SI Fig S4). Similar to NW3, two recrystallization fronts can be identified; predominantly along the [001] direction. A final anneal with a direct ramp to 400 °C followed by a temperature increase 500 °C was done to fully recover the crystallinity of the NW. Based on the HRTEM images acquired, in Figure 8 (f), no stacking fault defects were observed and this is attributed to the SPEG.

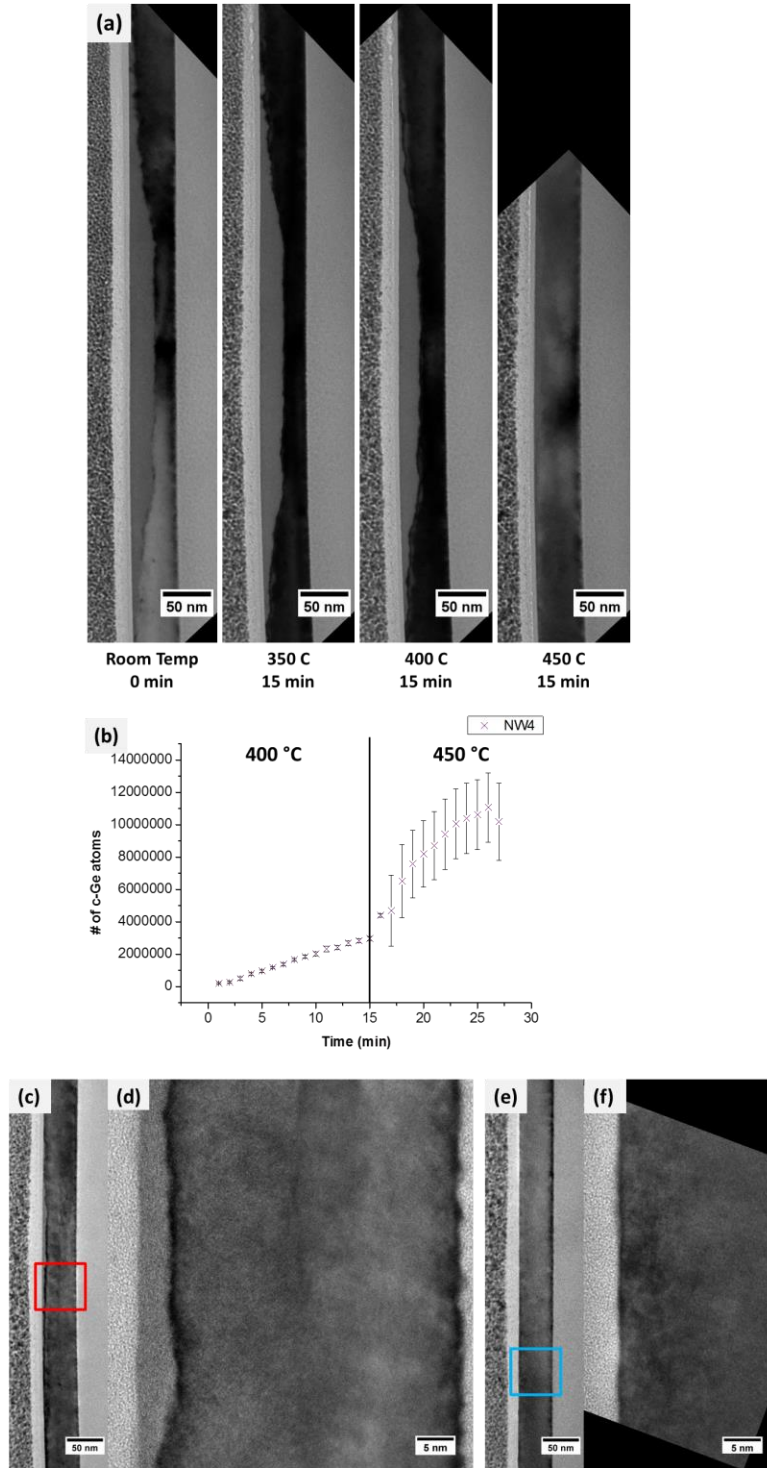


Figure 8. (a) In-situ anneal of Ge (001) NW4. The NW was heated incrementally from 100 °C to 450 °C in 50 °C increments and remaining at each temperature for 15 min. (b) Graphical representation of recrystallization of NW4 at 400 °C. Ge (001) NW4 (a) and (b) post-anneal. (c) and (d) after further anneal with a rapid ramp directly to 400 °C and then to 500 °C for 10 min.

Activation energies (E_a) in the range between 2.0 eV and 2.19 eV have been previously reported for Ge recrystallization.^{35, 42-45} To calculate the E_a of recrystallization in a NW, the rate of recrystallization of two different temperatures for the same NW were used, the calculation is described in the Supporting Information. For this report, NW4 was used to calculate a crude estimation of the E_a of recrystallization to be approximately 1.4 eV. Only this NW was used for the E_a calculation due to the slow ramp rate for both temperatures (400 and 450 °C) for the calculation and the abundant amorphous “sink” for both anneal temperatures, i.e. less than 50% of the volume recrystallized at the 400 °C. The contribution of the electron beam was not accounted for in the calculations of activation energy. The anneal of NW4 was initiated at 100 °C with recrystallization only observed from 400 °C. This would suggest that the electron beam had little or no effect on the recrystallization. The E_a obtained in MD simulations was 0.92 eV which confirms a slightly smaller value in comparison to simulations of planar recrystallization, where the activation energy was $E_a=1.09$ eV.³⁰

A notable difference between irradiated NWs and bulk substrates is the shape of the c/a interface. In a bulk substrate, the c/a interface may be rough but the interface is relatively flat so recrystallization occurs primarily in one direction. For a grown NW with a remaining crystal backbone the interface has two extra dimensions to consider – the crystal fronts created at the edge of the irradiated region and the curved cross sectional interface, as shown in Fig S3 in SI. Although the crystal backbone has proven successful in facilitating SPEG, any strain may result in misorientation, as seen in the suspended NWs, and hence defect formation. With an increase in rigidity, presence of crystal seed (backbone) and rectangular cross section, the top-down NW is more comparable with a bulk substrate.

CONCLUSION

A loss of ordering with amorphisation results in misorientation of crystal seeds in NWs due to deformation with decreasing rigidity. Although a NW is identified as a one-dimensional material it does have a three-dimensional structure and a TEM image gives a two-dimensional representation. Recrystallization also occurs not only in the growth direction, particularly for a (111) grown NW, but at all available crystal fronts. Recrystallization of a NW is complex due to the high surface area and hence sensitivity to any alteration to the surface, such as H infiltration.³⁶ (111) stacking fault pinning at the surface of the NW has been directly observed in this study. This result highlights the contributing factor that the surface-area to volume ratio has on NW recrystallization for both the rate and crystal structure. The effect of misorientation of crystal grains in NWs is minimized when the amorphisation is limited to allow a crystalline backbone and/or with external support in a matrix, promoting SPEG.

It has been observed that for $\langle 111 \rangle$ grown NWs, no defects form in the growth direction of the NW, i.e. no lateral (111) stacking faults are formed.⁴⁶ However, for the $\langle 112 \rangle$ grown NW containing intrinsic ($\bar{1}11$) longitudinal defects, extrinsic ($\bar{1}11$) defects in the same orientation as the intrinsic defects formed as well as $\langle 111 \rangle$ orientated stacking fault defects pinned to the surface. In other studies, a high temperature anneal has shown to cure extrinsic (111) stacking faults¹⁵ but a thermal budget for device fabrication may limit process temperatures. An alternative potential route for ion beam doping of nanostructures is moderate heating (approximately 250 °C) during irradiation which promotes dynamic annealing.⁴⁷ It is important to understand the recrystallization mechanism in NWs as device dimensions scale downwards and manipulation of NW properties on a large scale process becomes necessary.

REFERENCES

1. Moore, G. E., Lithography and the Future of Moore's law. *SPIE* **1995**, 2437.
2. Haynes, J. R.; Shockley, W., The mobility and life of injected holes and electrons in germanium. *Physical Review* **1951**, 81 (5), 835-843.
3. Paul, D. J., Si/SiGe heterostructures: from material and physics to devices and circuits. *Semiconductor Science and Technology* **2004**, 19 (10), R75-R108.
4. Huang, Y.; Duan, X. F.; Cui, Y.; Lauhon, L. J.; Kim, K. H.; Lieber, C. M., Logic gates and computation from assembled nanowire building blocks. *Science* **2001**, 294 (5545), 1313-1317.
5. Cui, Y.; Zhong, Z. H.; Wang, D. L.; Wang, W. U.; Lieber, C. M., High performance silicon nanowire field effect transistors. *Nano Letters* **2003**, 3 (2), 149-152.
6. Michel, J.; Liu, J.; Kimerling, L. C., High-performance Ge-on-Si photodetectors. *Nature Photonics* **2010**, 4 (8), 527-534.
7. Cui, Y.; Wei, Q. Q.; Park, H. K.; Lieber, C. M., Nanowire nanosensors for highly sensitive and selective detection of biological and chemical species. *Science* **2001**, 293 (5533), 1289-1292.
8. Tian, B.; Zheng, X.; Kempa, T. J.; Fang, Y.; Yu, N.; Yu, G.; Huang, J.; Lieber, C. M., Coaxial silicon nanowires as solar cells and nanoelectronic power sources. *Nature* **2007**, 449 (7164), 885-U8.
9. Yan, R.; Gargas, D.; Yang, P., Nanowire photonics. *Nature Photonics* **2009**, 3 (10), 569-576.
10. Kelly, R. A.; Holmes, J. D.; Petkov, N., Visualising discrete structural transformations in germanium nanowires during ion beam irradiation and subsequent annealing. *Nanoscale* **2014**, 6 (21), 12890-12897.
11. Zeiner, C.; Lugstein, A.; Burchhart, T.; Pongratz, P.; Connell, J. G.; Lauhon, L. J.; Bertagnolli, E., Atypical Self-Activation of Ga Dopant for Ge Nanowire Devices. *Nano Letters* **2011**, 11 (8), 3108-3112.
12. Yu, R.; Georgiev, Y. M.; Das, S.; Hobbs, R. G.; Povey, I. M.; Petkov, N.; Shayesteh, M.; O'Connell, D.; Holmes, J. D.; Duffy, R., Junctionless nanowire transistor fabricated with high mobility Ge channel. *physica status solidi (RRL) – Rapid Research Letters* **2014**, 8 (1), 65-68.
13. Guilloy, K.; Pauc, N.; Robin, E.; Calvo, V.; Gentile, P.; Foubert, K.; Rothman, J.; Reboud, V.; Chelnokov, A.; Benevent, V.; Hartmann, J. M. In *Band structure engineering of strained and doped germanium nanowires and 2D layers*, Group IV Photonics (GFP), 2014 IEEE 11th International Conference on, 27-29 Aug. 2014; 2014; pp 233-234.
14. Priolo, F.; Gregorkiewicz, T.; Galli, M.; Krauss, T. F., Silicon nanostructures for photonics and photovoltaics. *Nat Nano* **2014**, 9 (1), 19-32.
15. Duffy, R.; Shayesteh, M.; McCarthy, B.; Blake, A.; White, M.; Scully, J.; Yu, R.; Kelleher, A. M.; Schmidt, M.; Petkov, N.; Pelaz, L.; Marques, L. A., The curious case of thin-body Ge crystallization. *Applied Physics Letters* **2011**, 99 (13).
16. Jun, K.; Joo, J.; Jacobson, J. M., Focused ion beam-assisted bending of silicon nanowires for complex three dimensional structures. *Journal of Vacuum Science & Technology B* **2009**, 27 (6), 3043-3047.

17. Ronning, C.; Borschel, C.; Geburt, S.; Niepelt, R., Ion beam doping of semiconductor nanowires. *Materials Science & Engineering R-Reports* **2010**, *70* (3-6), 30-43.
18. Das Kanungo, P.; Koegler, R.; Zakharov, N.; Werner, P.; Scholz, R.; Skorupa, W., Characterization of Structural Changes Associated with Doping Silicon Nanowires by Ion Implantation. *Crystal Growth & Design* **2011**, *11* (7), 2690-2694.
19. Pecora, E.; Irrera, A.; Boninelli, S.; Romano, L.; Spinella, C.; Priolo, F., Nanoscale amorphization, bending and recrystallization in silicon nanowires. *Applied Physics A* **2011**, *102* (1), 13-19.
20. Fukata, N.; Takiguchi, R.; Ishida, S.; Yokono, S.; Hishita, S.; Murakami, K., Recrystallization and Reactivation of Dopant Atoms in Ion-Implanted Silicon Nanowires. *Acs Nano* **2012**, *6* (4), 3278-3283.
21. Grossklaus, K. A.; Banerjee, A.; Jahangir, S.; Bhattacharya, P.; Millunchick, J. M., Misorientation defects in coalesced self-catalyzed GaN nanowires. *Journal of Crystal Growth* **2013**, *371* (0), 142-147.
22. Romano, L.; Rudawski, N. G.; Holzworth, M. R.; Jones, K. S.; Choi, S. G.; Picraux, S. T., Nanoscale manipulation of Ge nanowires by ion irradiation. *Journal of Applied Physics* **2009**, *106* (11).
23. Borschel, C.; Spindler, S.; Lerose, D.; Bochmann, A.; Christiansen, S. H.; Nietzsche, S.; Oertel, M.; Ronning, C., Permanent bending and alignment of ZnO nanowires. *Nanotechnology* **2011**, *22* (18).
24. Gomez-Selles, J. L.; Darby, B. L.; Jones, K. S.; Martin-Bragado, I., Lattice kinetic Monte Carlo modeling of germanium solid phase epitaxial growth. *Physica Status Solidi C: Current Topics in Solid State Physics, Vol 11, No 1* **2014**, *11* (1), 93-96.
25. Darby, B. L.; Yates, B. R.; Martin-Bragado, I.; Gomez-Selles, J. L.; Elliman, R. G.; Jones, K. S., Substrate orientation dependence on the solid phase epitaxial growth rate of Ge. *Journal of Applied Physics* **2013**, *113* (3), -.
26. Pelaz, L.; Marques, L.; Aboy, M.; Lopez, P.; Santos, I.; Duffy, R. In *Atomistic process modeling based on Kinetic Monte Carlo and Molecular Dynamics for optimization of advanced devices*, Electron Devices Meeting (IEDM), 2009 IEEE International, 7-9 Dec. 2009; 2009; pp 1-4.
27. Hobbs, R. G.; Schmidt, M.; Bolger, C. T.; Georgiev, Y. M.; Fleming, P.; Morris, M. A.; Petkov, N.; Holmes, J. D.; Xiu, F. X.; Wang, K. L.; Djara, V.; Yu, R.; Colinge, J. P., Resist-substrate interface tailoring for generating high-density arrays of Ge and Bi₂Se₃ nanowires by electron beam lithography. *Journal of Vacuum Science & Technology B* **2012**, *30* (4).
28. Ran, Y.; Das, S.; Hobbs, R.; Georgiev, Y.; Ferain, I.; Razavi, P.; Akhavan, N. D.; Colinge, C. A.; Colinge, J. In *Top-down process of Germanium nanowires using EBL exposure of Hydrogen Silsesquioxane resist*, Ultimate Integration on Silicon (ULIS), 2012 13th International Conference on, 6-7 March 2012; 2012; pp 145-148.
29. Plimpton, S., Fast Parallel Algorithms for Short-Range Molecular Dynamics. *Journal of Computational Physics* **1995**, *117* (1), 1-19.
30. Posselt, M.; Gabriel, A., Atomistic simulation of amorphous germanium and its solid phase epitaxial recrystallization. *Physical Review B* **2009**, *80* (4).
31. Luedtke, W. D.; Landman, U., Preparation, structure, dynamics, and energetics of amorphous silicon: A molecular-dynamics study. *Physical Review B* **1989**, *40* (2), 1164-1174.
32. Berendsen, H. J. C.; Postma, J. P. M.; van Gunsteren, W. F.; DiNola, A.; Haak, J. R., Molecular dynamics with coupling to an external bath. *The Journal of Chemical Physics* **1984**, *81* (8), 3684-3690.

33. Kelly, P. M.; Wauchope, C. J.; Zhang, X., Calculation of overall tilt angles for a double tilt holder in a TEM. *Microscopy Research and Technique* **1994**, 28 (5), 448-451.
34. Priolo, F.; Battaglia, A.; Nicotra, R.; Rimini, E., Low-temperature reordering in partially amorphized si crystals. *Applied Physics Letters* **1990**, 57 (8), 768-770.
35. Csepregi, L.; Küllen, R. P.; Mayer, J. W.; Sigmon, T. W., Regrowth kinetics of amorphous Ge layers created by ⁷⁴Ge and ²⁸Si implantation of Ge crystals. *Solid State Communications* **1977**, 21 (11), 1019-1021.
36. Johnson, B. C.; Gortmaker, P.; McCallum, J. C., Intrinsic and dopant-enhanced solid-phase epitaxy in amorphous germanium. *Physical Review B* **2008**, 77 (21), 214109.
37. Borschel, C.; Ronning, C., Ion beam irradiation of nanostructures - A 3D Monte Carlo simulation code. *Nuclear Instruments & Methods in Physics Research Section B-Beam Interactions with Materials and Atoms* **2011**, 269 (19), 2133-2138.
38. den Hertog, M. I.; Cayron, C.; Gentile, P.; Dhalluin, F.; Oehler, F.; Baron, T.; Rouviere, J. L., Hidden defects in silicon nanowires. *Nanotechnology* **2012**, 23 (2).
39. Barth, S.; Boland, J. J.; Holmes, J. D., Defect Transfer from Nanoparticles to Nanowires. *Nano Letters* **2011**, 11 (4), 1550-1555.
40. Drosd, R.; Washburn, J., Some observations on the amorphous to crystalline transformation in silicon. *Journal of Applied Physics* **1982**, 53 (1), 397-403.
41. Olson, G. L.; Roth, J. A., Kinetics of solid phase crystallization in amorphous silicon. *Materials Science Reports* **1988**, 3 (1), 1-77.
42. Donovan, E. P.; Spaepen, F.; Turnbull, D.; Poate, J. M.; Jacobson, D. C., Calorimetric studies of crystallization and relaxation of amorphous Si and Ge prepared by ion implantation. *Journal of Applied Physics* **1985**, 57 (6), 1795-1804.
43. Lu, G. Q.; Nygren, E.; Aziz, M. J., Pressure-enhanced crystallization kinetics of amorphous Si and Ge: Implications for point-defect mechanisms. *Journal of Applied Physics* **1991**, 70 (10), 5323-5345.
44. Haynes, T. E.; Antonell, M. J.; Lee, C. A.; Jones, K. S., Composition dependence of solid-phase epitaxy in silicon-germanium alloys: Experiment and theory. *Physical Review B* **1995**, 51 (12), 7762-7771.
45. Kringhøj, P.; Elliman, R. G., Solid-phase epitaxial crystallization of strain-relaxed Si_{1-x}Ge_x alloy layers. *Physical Review Letters* **1994**, 73 (6), 858-861.
46. Geaney, H.; Dickinson, C.; Weng, W. H.; Kiely, C. J.; Barrett, C. A.; Gunning, R. D.; Ryan, K. M., Role of defects and growth directions in the formation of periodically twinned and kinked unseeded germanium nanowires. *Crystal Growth & Design* **2011**, 11 (7), 3266-3272.
47. Posselt, M.; Bischoff, L.; Grambole, D.; Herrmann, F., Competition between damage buildup and dynamic annealing in ion implantation into Ge. *Applied Physics Letters* **2006**, 89 (15).

ASSOCIATED CONTENT

Supporting Information.

Details of inline NW FIB sample preparation, example of measurement of growth of crystal region, equation for relative angle between crystal orientations, example of irradiated grown NW cross section, example of EBL defined NW cross section, details of limitation of exposure times for TEM. This material is available free of charge via the Internet at <http://pubs.acs.org>.

AUTHOR INFORMATION

Corresponding Author

*E-mail: nikolay.petkov@tyndall.ie; Tel: +353 214205713

Author Contributions

The manuscript was written through contributions of all authors. All authors have given approval to the final version of the manuscript.

ACKNOWLEDGMENT

This work was supported principally by Science Foundation Ireland (SFI) under the Starting Investigator Research Grant (SIRG) under Contract No. 09/SIRG/I1623 and the Principal Investigator Program under Contract No. 09/IN.1/I2602 and by Deutsche Forschungsgemeinschaft under Grant Nos. BR 1520/14-1.